Interface-Engineered $Li_7La_3Zr_2O_{12}$-Based Garnet Solid Electrolytes with Suppressed Li-Dendrite Formation and Enhanced Electrochemical Performance

Zhang, Zhaoshuai; Zhang, Long; Liu, Yanyan; Wang, Hongqiang; Yu, Chuang; Zeng, Hong; Wang, Li min; Xu, B.

DOI
10.1002/cssc.201801756

Publication date
2018

Document Version
Accepted author manuscript

Published in
ChemSusChem

CHEMISTRY & SUSTAINABILITY

CHEMSUSCHEM

ENERGY & MATERIALS

Accepted Article

Title: Interface-Engineered Li7La3Zr2O12-Based Garnet Solid Electrolytes with Suppressed Li dendrite Formation and Enhanced Electrochemical Performance

Authors: Zhaoshuai Zhang, Long Zhang, Yanyan Liu, Hongqiang Wang, Chuang Yu, Hong Zeng, Li-min Wang, and Bo Xu

To be cited as: *ChemSusChem* 10.1002/cssc.201801756

Link to VoR: http://dx.doi.org/10.1002/cssc.201801756

A Journal of

ChemPubSoc Europe

WILEY-VCH

www.chemsuschem.org

Interface-Engineered $Li_7La_3Zr_2O_{12}$-Based Garnet Solid Electrolytes with Suppressed Li dendrite Formation and Enhanced Electrochemical Performance

Zhaoshuai Zhang,[1] Long Zhang,[1*] Yanyan Liu,[1] Hongqiang Wang,[2] Chuang Yu,[3] Hong Zeng,[4] Li-min Wang,[1] Bo Xu[1]

[1]State Key Laboratory of Metastable Materials Science and Technology, Yanshan University, Qinhuangdao, Hebei 066004, China

[2]College of Chemistry & Environmental Science, Hebei University, Baoding, Hebei 071000, China

[3]Department of Radiation Science and Technology, Delft University of Technology, Mekelweg 15, Delft 2629 JB, The Netherlands

[4]Beijing Key Laboratory of Energy Nanomaterials, Advance Technology & Materials Co., Ltd, China Iron & Steel Research Institute Group, Beijing 100081 , China

ABSTRACT

Large grain boundary resistance, Li dendrite suppression, and interfacial resistance of electrode/Li are three major issues against garnet-based solid electrolytes. Herein, we propose an interfacial architecture engineering by incorporating BMP-TFSI ionic liquid into the garnet oxide. The “soft” consecutive BMP-TFSI coating layer with no added Li-salt raises a conducting network facilitating Li^+ transport and thus changes the ion conduction mode from point contacts to face contacts; a compacted microstructure to suppress the Li dendrite growth; a good interfacial compatibility and interfacial wettability toward metallic Li. Along with an broad electrochemical window over 5.5 V and a Li^+ transference number practically reaching unity, the NCM811/Li and $LiFePO_4$/Li solid batteries with the hybrid solid electrolyte exhibit superior cycling stability and low polarization comparable to those with commercial

liquid electrolytes, and excellent rate capability better than those with Li-salt-based ionic liquid electrolytes.

KEYWORDS: $Li_7La_3Zr_2O_{12}$; garnet; ionic liquid; interface; all-solid-state lithium ion batteries

1. INTRODUCTION

Lithium-ion batteries (LIBs) with high energy density and potentially long cycle life have attracted broad attention in rechargeable chemical energy storage devices such as, cell phones, laptops, and electric vehicles.[1] Conventional LIBs with organic liquid electrolyte raise the safety concerns regarding leak and flammability. In addition, the intrinsic shortcoming of liquid electrolyte such as high toxicity, narrow electrochemical stability window, and low thermal stability limits their applications.[2] One of the promising ways to solve these problems is to replace liquid electrolyte with solid electrolyte (SE), which possesses high thermal stability, wide electrochemical window, and is suitable for direct-stacking technique.[3]

As a series of promising inorganic SEs, the lithium garnet-type $Li_7La_3Zr_2O_{12}$, discovered by Thangadurai and Weppner in 2007,[4] has been intensively studied because of its high chemical stability, wide electrochemical stability window, good mechanical properties, and relatively high ionic conductivity.[5] The major challenges for the practical use of garnet-type SEs in all-solid-state LIBs (ASLIBs) include:[3a, 3e, 5d, 6] 1) the large interfacial resistance between SE and electrode due to the rigid ceramic nature of $Li_7La_3Zr_2O_{12}$ and formation of Li_2CO_3 by air absorption; 2) poor interfacial wetting between Li metal and $Li_7La_3Zr_2O_{12}$ preventing the intimate physical contact; and 3) formation of Li dendrite due to uneven deposition of Li metal, which may penetrate the SE and short batteries. Additionally, the rigid nature of the oxide electrolyte causes a very poor contact between cathode and electrolyte, thus leading to a large interfacial resistance. Consequently, the cell polarization at the

garnet/metallic Li interface is enlarged and increases with cycling time and current density.[7]

Another shortcoming is that $Li_7La_3Zr_2O_{12}$ needs a long term sintering (typically over 12 hours) at high temperature (1100–1250 °C) to obtain a cubic structure and tight grain boundaries, which are prerequisite for a high ionic conductivity.[5a] Although tetragonal $Li_7La_3Zr_2O_{12}$ ($I4_1/acd$, No. 142)[8] is easier to be stabilized at room temperature, it has a smaller ionic conductivity in contrast to the cubic structure (Ia-3d, No. 230).[9] Generally, high temperature sintering process can cause Li volatilization and compositional deviations.

The next generation high-energy batteries are likely to compose a hybrid pseudo solid electrolyte with trace of liquid electrolyte,[10] which can effectively reduce the interfacial resistance and enhance the interfacial stability. Ionic liquids (ILs), characterized by intrinsic ionic conductivity, good thermal stability, nonvolatility, and non-flammability can effectively improve the safety performance of batteries.[11] ILs have been widely studied and are recognized as safe electrolytes for high-energy-density LIBs.[12] Therefore, it is a friendly additive for hybrid solid electrolytes. ILs were usually used together with Li-salt (e.g. LiTFSI) as a liquid electrolyte. However, dissolving lithium salt into IL inevitably leads to enhanced ionic bonds in the mixture, which increases the viscosity and hence affects the ionic mobility.[13] The increased viscosity will change the interaction between Li^+ and $TFSI^-$, which forms ion pairs and ion aggregation with different chemical properties.[14] High viscosity not only limits ionic transference numbers but also has an adverse effect on

the conductivity.[13] Therefore, pure IL with no added Li-salt is preferred as an additive. Among various IL materials, 1-Butyl-1-methylpyrrolidinium bis(trifluoromethylsulfonyl) imide (BMP-TFSI) is very attractive because it can effectively stabilize superoxide anion radicals and has good stability toward metallic Li. [15] Compared to other types of ILs, the ring structure of BMP-TFSI is close to flat with less resistance to movement, lower viscosity, and higher ionic conductivity.[16] In addition, its cathodic stability limit (associated with the reduction of BMP^+) is beyond the Li plating/stripping reaction and $TFSI^-$ can withstand a high potential (>5.5 V vs. Li).[17]

In this study, we address the challenge of the interfacial resistance by introducing an IL phase on the surface of garnet particle to form a hybrid electrolyte. IL containing no added Li-salt to ensure high Li^+ transference numbers and maintain low viscosity to facilitate Li-ion transport ability. The ceramic oxide powders are uniformly wetted with appropriate amount of IL to improve the surface wettability and stability of electrolyte/electrode, and hence significantly enhances the interfacial compatibility and decreases the interfacial resistance of electrolyte/Li. By avoiding high temperature sintering, this unique type of hybrid solid electrolyte (HSE) succeeds in increasing ionic conductivity and achieving high Li^+ transference number. Based on this particular interface-engineered HSE, solid state $LiFePO_4$/Li and $LiNi_{0.8}Co_{0.1}Mn_{0.1}O_2$/Li batteries exhibit excellent electrochemical performance and cycling stability.

2. EXPERIMENTAL SECTION

2.1. Sample preparation

Cubic garnet $Li_{6.75}La_3Zr_{1.75}Ta_{0.25}O_{12}$ (LLZO) powders were synthesized by conventional solid state reaction. The starting materials Li_2CO_3 (Aladdin reagent, 99.99%), La_2O_3 (Aladdin reagent, 99.99%), ZrO_2 (Aladdin reagent, 99.99%), $TaCl_5$ (J&K Chemical, 99.99%) and Al_2O_3 (Aladdin reagent, 99.99%) powders were weighed and mixed in stoichiometric amounts with the molar ratio of Li:La:Zr:Ta to be 6.75:3:1.75:0.25. A proper amount of Al_2O_3 was added to obtain a doping level of 0.24 mole of Al in one unit formula of garnet. Al and Ta co-doping is beneficial to stabilize the high conductivity cubic structure at room temperature and thus reduces the sintering temperature. A 10 wt% excess of Li_2CO_3 was used to compensate Li volatilization during synthesis. The mixed precursors were placed in a tungsten carbide vial and ball-milled in Ar atmosphere for 8 h with a rotational speed of 150 rpm. The resulting mixture was calcinated in air atmosphere at 900 °C for 5 h in an alumina crucible at a heating rate of 2 °C/min. The resulting powders were then ball-milled for 2 h to refine the particle size. The final powders were sieved using a 45 μm mesh.

The prepared LLZO powders and BMP-TFSI (J&K Chemical, 99%) IL were mixed in various mass ratio and ground thoroughly and uniformly in a mortar. Then the homogenized blended mixture was cold pressed into pellets under an axial pressure of 15 MPa for 2 minutes. As a comparison, the pristine LLZO dry powders were also cold pressed under the same conditions. All procedures were carried out in an argon-filled glove box with H_2O, O_2<0.5ppm.

2.2. Materials Characterization

X-ray powder diffraction (XRD) was performed using a Rigaku D/MAX-2500/PC (Cu Kα, 40 kV 200 mA) from 10 to 60° with a step size of 0.02°. Morphological characterizations were analyzed with a scanning electron microscope (SEM, Hitachi S-4800 II FESEM) equipped with an energy dispersive spectrometry (EDS). Raman scattering measurements were performed using a Renishaw inVia system with a 785 nm excitation source. Fourier transform infrared (FTIR) spectra were recorded with a E55+FRA106 instrument at ambient temperature from 500−4000 cm^{-1}. Thermogravimetric analysis (TGA) measurements were carried out on a Netzsch STA thermoanalyzer from room temperature to 600 °C with a heating rate of 5 °C/min in an argon atmosphere.

2.3. Electrochemical Characterization

AC impedance measurements were performed in the frequency range of 0.1 Hz–3 MHz at ambient temperature with an impedance analyzer (Princeton P4000; Princeton Applied Research, Oak Ridge, TN). Indium foil was placed on both sides of the pellets, and then mounted on an air-tight two-electrode cell with two stainless-steel (SS) rods as current collectors. Samples were assembled in an Ar-filled glove box to avoid moisture contamination. Linear sweep voltammetry (LSV) was measured on Li/SE/SS cells using Princeton P4000 at a scanning rate of 1 mV/s, where SS and Li were respectively used as the working and counter/reference electrode. Wagner's polarization measurements were performed at room temperature to determine the electronic contribution to the total conductivity on a SS/SE/Li cell. The cell was

polarized by applying a constant dc potential (Princeton P4000) from 2 to 5 V.

The electrochemical performance of solid state batteries was tested on a Land charge/discharge instrument (Wuhan Rambo Testing Equipment Co., Ltd.) by assembling 2032 coin-type cells with a $LiFePO_4$ or $LiNi_{0.8}Co_{0.1}Mn_{0.1}O_2$ (NCM811) positive electrode and a lithium metal negative electrode. The cells were fabricated as follows. The positive electrode was prepared by mixing 80 wt% NCM811 or $LiFePO_4$ active material, 10 wt% carbon black, and 10 wt% Poly(vinylidene fluoride) (PVDF), dissolved in N-methylpyrrolidinone (NMP). The resulting slurry was pasted onto carbon-coated aluminum foil and dried at 100 °C for 12 h under vacuum. The mass loading of the active material (NCM811 or $LiFePO_4$) on the electrode is ~1.5 mg/cm^2. Approximately 12 μL commercial liquid electrolyte was added to the positive electrode to reduce the interfacial resistance of cathode/electrolyte. The electrochemical stability of the $LiFePO_4$/SE/Li cell was evaluated via cyclic voltammetry (CV) using a Princeton P4000 instrument from 2.0 to 5.0 V with a scan rate of 2 mV/s.

3. RESULTS AND DISCUSSION

3.1. Ionic Conductivity and Microstructure of the HSEs

Figure 1a displays the room temperature Nyquist plot of the pristine LLZO sample with Au as blocking electrodes. A semicircle and Warburg-type impedance were observed in the high and low frequency regions, respectively. This is in accordance with the results previously reported.[18] The semicircle is assigned to the boundary and void contributions; the intercept of the semicircle with real axis at high frequency can

be attributed to the bulk resistance. The conducting behavior was modeled using the equivalent circuit $R_b(R_{gb}CPE_{gb})CPE_{el}$ (inset of Figure 3a), where R is the resistance, CPE is the constant phase element, and the subscripts b, gb, and el represent the bulk, grain boundary, and electrode contribution, respectively.[19] The bulk and grain boundary resistance of LLZO were calculated to be 1200 and 1.36×10^5 Ω, respectively, indicating a grain boundary dominated conduction.

Figure 1b shows the impedance spectrum of BMP-TFSI, which was measured on a cell with In as the electrodes and Celgard 2400 as the separator absorbed with BMP-TFSI electrolyte. Calculated from the total resistance, the room temperature conductivity is ~1 mS/cm. One should be reminded that this value may be contributed by both anions and cations. By incorporating BMP-TFSI, the ionic conductivity (σ) of the HSEs is several orders of magnitude higher than that of pristine LLZO. As listed in Table 1, the ionic conductivity of the HSEs increases with increasing BMP-TFSI concentration. However, it is difficult to shape the pellet when the amount of BMP-TFSI higher than 21 wt%. The HSE with 14 wt% BMP-TFSI (designated as LLZO-IL) is thus selected for further investigation due to its good formability and relative high ionic conductivity. Figure 1c shows the impedance spectrum of LLZO-IL. The semicircle at high frequency nearly disappears compared with the pristine LLZO sample, indicating a negligible grain boundary resistance. Since the semicircle at high frequency is too few to separate the grain boundary contribution, the ionic conductivity of the BMP-TFSI and LLZO-IL samples was calculated from the total resistance. This is a common calculating method for those superionic

conductors with bulk-dominated overall resistance.[20] The ionic conductivity of LLZO-IL is 0.67 mS/cm, three orders of magnitude higher than pristine LLZO (4.5×10^{-4} mS/cm). The steep linear spike at low frequency indicates that LLZO-IL is a typical ion conductor. This result reveals that the anions of BMP-TFSI in LLZO-IL HSE is fixed or maintains a negligible movement.

Table 1. The effect of BMP-TFSI IL on the formability and ionic conductivity of LLZO-based HSEs.

LLZO (wt%)	BMP-TFSI (wt%)	Form	Ionic conductivity (mS/cm)
100	0	solid	~10^{-4}
95	5	solid	0.43
90	10	solid	0.47
86	14	soft solid	0.67
84	16	soft solid	0.78
79	21	gel-like	1.3
75	25	mud-like	>1.3

The significant increase in ionic conductivity of the HSEs is attributed to the decrease in grain boundary resistance by incorporating IL into LLZO particles. As illustrated in Figure 1d, the high ionic conductivity of the HSEs indicates that Li^+ in LLZO can easily transfer between the solid/liquid interfaces and inside BMP-TFSI, which acts as a binder/filler connecting LLZO particles. The consecutive BMP-TFSI coating layer forms a conducting network facilitating Li ions across the particle boundaries. As a result, Li^+ conduction mode changes from point contacts in pristine LLZO to face contacts in the HSEs. IL individually in HSE takes responsibility for

ensuring a fast ion conduction. Since the addition of LiTFSI increases the viscosity of IL and introduces the $TFSI^-$ anions, Li-salt is no need in such a coating layer system.

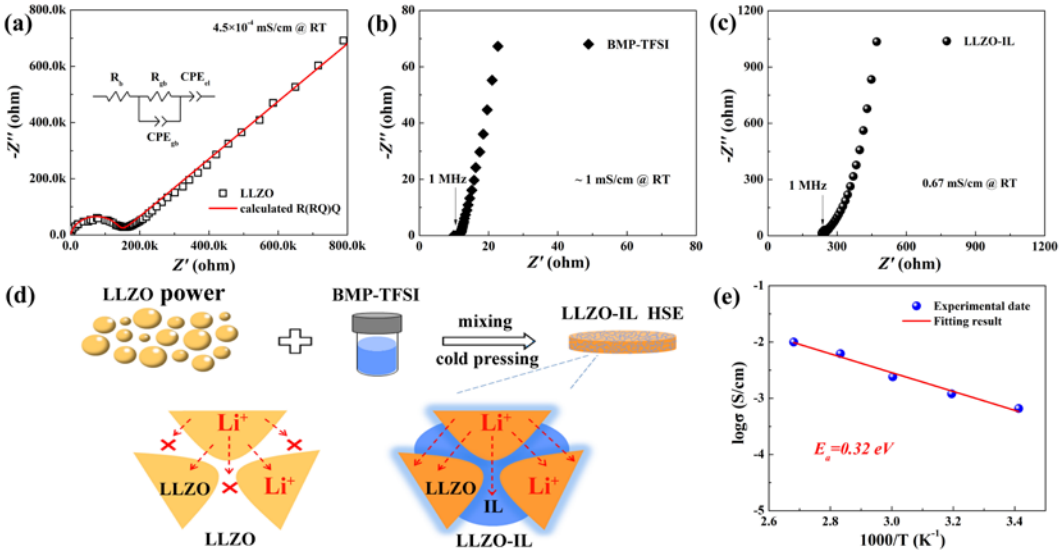

Figure 1. Impedance spectra measured at room temperature for the pristine LLZO sample (a), BMP-TFSI ionic liquid (b), and LLZO-IL HSE (c). (d) Schematic illustration of different Li^+ transferring mechanism in LLZO and LLZO-IL. (e) Arrhenius conductivity plot of LLZO-IL from 20 °C to 100 °C.

The consecutive BMP-TFSI coating layer was confirmed by observing the morphology of the selected samples. Representative cross-sectional images of LLZO and LLZO-IL are shown in Figure 2. The samples were fractured and no additional polishing or etching was performed after fracturing. Significant amount of open porosity are observed between the grains in the pristine LLZO sample (Figure 2a,b). It has a low relative density (67%), resulting in low ionic conductivity. In contrast, BMP-TFSI in LLZO-IL HSE forms a consecutive coating layer on LLZO and thus no pore is observed (Fig. 2c,d). The role of BMP-TFSI likes a binder to compact the

structure. The relative density of LLZO-IL is approximate 81%, significantly higher than that of pristine LLZO. This homogenous and thin IL layer is favorable to provide a conducting pathway for lithium ion transport (Figure 1d). EDS analyses were performed on the grain and the coating layer between grains to evaluate their difference on chemical composition, as depicted in Fig. 2e,f. Compared the atomic percentage (Fig. 2f) at the positions of EDS1 with EDS2, the latter shows a significantly higher concentration on C, F, and S, confirming the distribution of BMP-TFSI on the surface of LLZO particles.

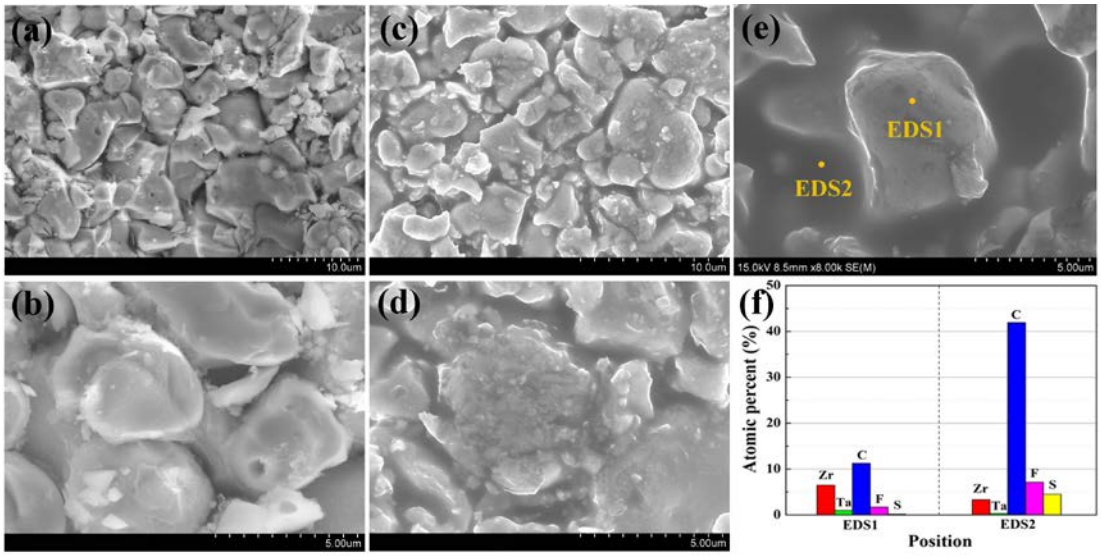

Figure 2. Cross-sectional SEM images of LLZO (a-b) and LLZO-IL (c-d). (e) EDS measurements on selected area. The points marked as EDS1 and EDS2 highlight the locations of the EDS measurements. (f) The histograms of elemental proportion for La, Ta, C, F, S detected at EDS1 and EDS2.

The reciprocal temperature dependence of the ionic conductivity of LLZO-IL HSE from 20 °C to 100 °C is shown in Figure 1e. The linear dependence of logσ vs. (1/T) follows the Arrhenius law and indicates phase stability over the measured temperature

range. The ionic conductivity of the HSE locates in the range from 0.67 mS/cm at 20 °C to 10 mS/cm at 100 °C. The activation energy E_a was determined from the slope of the linear Arrhenius plot using the equation: $\sigma = \sigma_0 \exp(-E_a/k_B T)$, where σ_0 is the pre-exponential parameter and k_B is the Boltzmann constant. The calculated activation energy of LLZO-IL electrolyte is E_a = 0.32 eV. This is a relatively low value among garnet solid electrolytes.

3.2. Structural Characterization and Thermal Stability of the Garnet HSEs

The XRD patterns of LLZO-IL HSE and the pristine LLZO sample are shown in Figure 3a. No significant structural change is observed after incorporating BMP-TFSI into LLZO. All diffraction peaks are well-matched with cubic garnet structure. The identical XRD profile before and after IL incorporation indicates that no obvious reaction and no Li^+/H^+ exchange occurs by adding aqueous BMP-TFSI IL.[21]

Raman and FTIR spectra were collected to further clarify the influence of IL incorporation on LLZO. Figure 3b shows Raman spectra of LLZO and LLZO-IL. All peaks in the pristine LLZO sample can be indexed to the cubic garnet phase.[22] Several observations can be made after BMP-TFSI incorporation. First, it appears a new peak located at 275 cm^{-1}, which is attributed to the vibrational frequency of $TFSI^-$.[23] Second, the peak intensity at ~750 cm^{-1} becomes higher than that of the pristine LLZO sample due to the overlap of the BMP-TFSI peak located at ~745 cm^{-1}.[23-24] Third, the relative intensity of the peaks at 355 cm^{-1} and 400 cm^{-1} changes. These results indicate that there is no significant chemical reaction between LLZO and BMP-TFSI. Considering the change of the relative intensity at 400 cm^{-1},

interaction between BMP-TFSI and LLZO may occur due to slight dissolution of the latter.[25] A small peak assigned to Li_2CO_3 can be observed at 1090 cm^{-1} in the Raman spectrum for pristine LLZO. The presence of Li_2CO_3 is unavoidable during LLZO preparation.[26] In contrast, the peak at 1090 cm^{-1} is hard to be seen for the LLZO-IL sample.

The FTIR spectra before and after IL incorporation are displayed in Figure 3c. For both samples, the peaks at 3450 cm^{-1} are observed, which can be assigned to the H-O bonds in absorbed water on the pellet surface.[27] This is inevitable because the FTIR measurements were carried in air. For the pristine LLZO sample, V_{as}(C=O) bonds at 1438 cm^{-1} and 863 cm^{-1} matched well with the Li_2CO_3 spectrum.[28] However, these two peaks are intensively suppressed in the LLZO-IL sample, due to the protection of the LLZO surface by IL coating. The peak observed at 1350 cm^{-1} is assigned to the SO_2 groups.[29] The major characteristic peaks of imide ions $TFSI^-$ are corresponding to the CF_3 symmetric stretching at 1200 cm^{-1}, C–SO_2–N stretching at 1140 cm^{-1}, and S–N–S asymmetric stretching at 1058 cm^{-1}.[30] The $\delta(H_2O)$ bond at 1640 cm^{-1} is induced by adsorbed water. These results confirm the stability between LLZO and BMP-TFSI IL, in accordance with XRD and Raman results.

Thermal stability of an electrolyte is a critical prerequisite for the safety and stability of a battery. The thermal behaviors of LLZO-IL and pristine LLZO were investigated by DTA measurements, as illustrated in Figure 3d. LLZO is stable over the measured temperature range up to 600 °C, indicating negligible water absorption on pristine LLZO. LLZO-ILZ is stable until 350 °C, where a weight loss of 8.4% is

detected. This is attributed to the decomposition of BMP-TFSI,[11c, 24] as revealed by the exothermic peak at ~400 °C in the DSC curve (inset of Figure 3d). LLZO-IL HSE is thus applicable in medium temperature area.

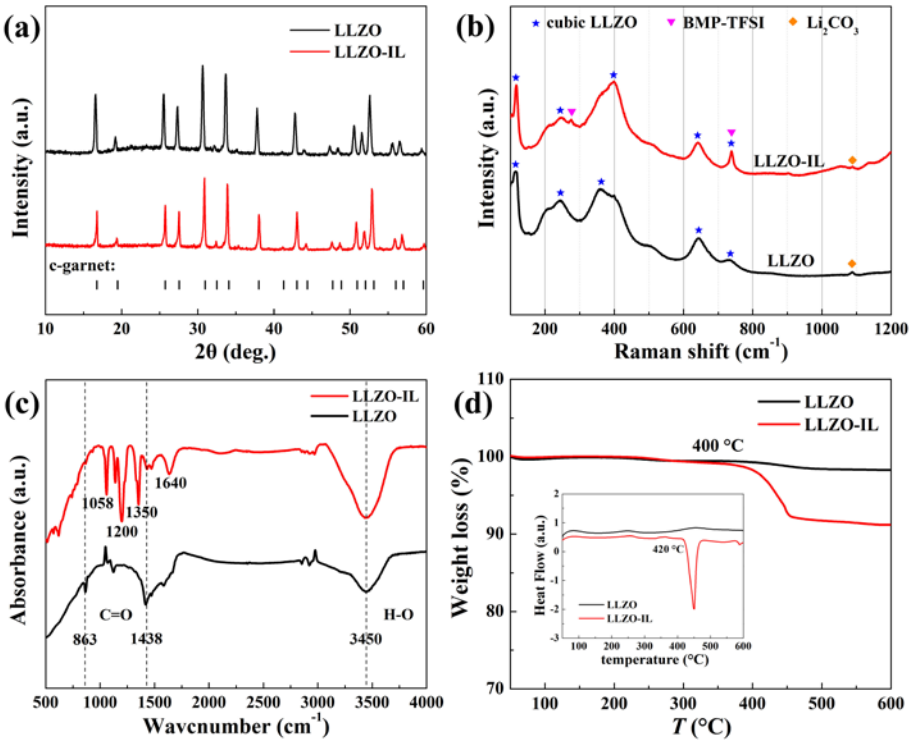

Figure 3. (a) XRD patterns of LLZO powders and LLZO-IL pellet. Raman (b) and FTIR (c) spectra of LLZO and LLZO-IL. (d) TGA curves of LLZO and LLZO-IL. The inset shows the DSC profiles of LLZO and LLZO-IL.

3.2. Electrochemical and Interfacial Performance of the Garnet HSEs

LSV measurements were performed in SS/Li cells using various electrolytes to investigate the electrochemical window. As shown in Figure 4a, the anodic current started to increase at 3.2 V for the cell with pure IL electrolyte because of the oxidative decomposition of BMP-TFSI. Although incorporation of BMP-TFSI reduces the stability window of LLZO, LLZO-IL HSE still exhibits a stable oxidative voltage over 5.5 V vs. Li^+/Li. This electrochemical window is broad enough for high

voltage cathodes.

A solid electrolyte normally involves dominant ions (σ_{Li+} for lithium ionic conductors) and minor electrons/holes ($\sigma_{(e+h)}$). The total conductivity comprises an ionic and an electronic part. Hebb-Wagner polarization measurements were carried out at room temperature to determine the Li^+ transference number of LLZO-IL.[31] Figure 4b shows the current–voltage characteristics on a Li/LLZO-IL/SS cell with the potential range from 2 to 3.5 V. The electronic conductivity was determined based on the equation: $\sigma_{(e+h)} = (L/S)(d|I_{e,h}|/dE)$, where $|I_{e,h}|$ is the total electronic current, E is the polarization voltage, S is the electrolyte–electrode surface area, and L is the electrolyte thickness.[32] Consequently, the calculated value of $\sigma_{(e+h)}$ is 9.6×10^{-9} S/cm. With the total conductivity of 0.67 mS/cm, the Li^+ transference number was determined to be 0.99998. This result confirms that 1) LLZO-IL is a pure ion conductor, as LLZO does; 2) $TFSI^-$ anions are fixed inside BMP-TFSI and do not participate in the conduction.

The critical current density, defined as the current segment value where the voltage drop occurred, is generally adopted to evaluate the dendrite suppression capability in an electrolyte.[33] Figure 4c illustrates the galvanostatic cycling of the LLZO-IL/Li cell tested at step-increased current densities. The step size of the current density was set to 0.03 mA/cm^2 with a duration of 30 min for each charge/discharge process. The positive and the negative voltages are respectively relevant to the Li stripping and plating processes. The critical current density is over 0.74 mA/cm^2. No short circuit is observed during the measurement. Unfortunately, the measurement was stopped

because the large overpotential exceeded the voltage limit of the instrument. Kotobuki et al. reported that the voltage intensively increased after keeping the symmetric cell for 70 s even at a current density as low as 0.05 mA/cm^2.[34] The large polarization originates from the loss of contact on electrolyte/Li electrode thus increasing interfacial resistance, which is a common issue in garnet electrolytes because of the poor contact wettability and lack of interphase between Li and garnet.[35] The AC impedance measurements (Figure S1) confirms the intensively increased resistance after cycling at step-increased current densities. The intensively increased resistance after testing at 0.74 mA/cm^2 can be understood by two aspects. On one hand, high current density cycling results in larger Li plating/stripping quantity and thus severer volume change. On the other hand, large overpotential may lead to side reaction between electrolyte and electrodes, which in turn increases resistance. Nevertheless, even with the testing interruption, the current density loaded in this work is significantly higher than the values reported previously for other garnet-type solid electrolytes.[36] Long term LLZO-IL/Li symmetrical cell tested at a current density of 0.1 mA/cm^2 at room temperature is shown in Figure 4d. The voltage polarization is stable at 0.17 V for more than 300 cycles without short circuit. The schematic illustration for the role of BMP-TFSI on HSE is depicted in Figure 4e. From the mechanical perspective, the “soft” BMP-TFSI consecutive coating layer, filling the voids and connecting the grain boundaries, is easy to form intimate contacts with the “rigid” LLZO oxide and maintain good interfacial compatibility toward metallic lithium.[37] Therefore, on one hand, the coating layer can form a compact and stable

interlayer to resist the volume strain at the electrolyte/electrode interface and inside the HSE during cycling.[38] On the other hand, As the short circuit is attributed to the growth of lithium dendrites along the grain boundaries and voids of the electrolyte,[3e, 39] the coating layer gives a uniform Li-ion flux through the interface and thus is effective to suppress Li dendrite growth.[40] It is worth noting that the LLZO powders in this work was sintered for only one time at 900 °C. No second sintering at 1200 °C was performed as other works did. A better dendrite suppression capability could be achieved with LLZO sintered at 1200 °C.

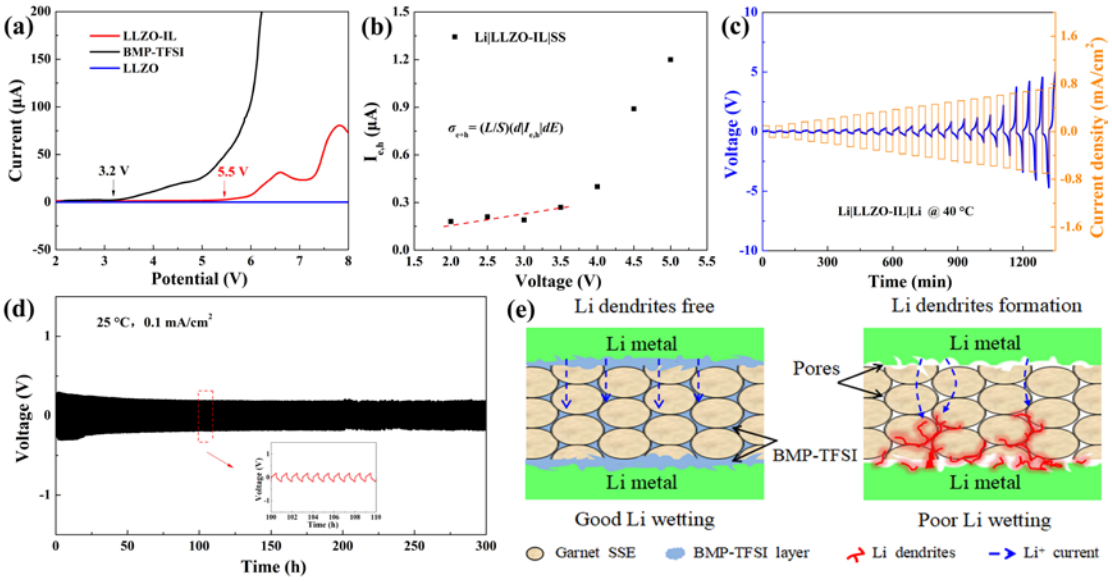

Figure 4. (a) LSV curves of the Li/LLZO-IL/SS cell compared with those of the Li/LLZO/SS and Li/BMP-TFSI/SS cells. (b) Wagner's polarization curve measured on a Li/LLZO-IL/SS cell at room temperature. (c) The Li/LLZO-IL/Li symmetric cell tested at 25 °C with step-increased current densities from 0.1 to 0.74 mA/cm^2. The time interval was set to 30 min for a charge or discharge run. (d) Galvanostatic cycling on a Li/LLZO-IL/Li symmetric cell with a current density of 0.1 mA/cm^2 at room temperature. (e) Schematic illustration for the role of BMP-TFSI coating layer.

3.3. Electrochemical Performance of HSE-Based Solid State Batteries

Solid state NCM811/Li and $LiFePO_4$/Li batteries with LLZO-IL HSE were set up to evaluate the stability of HSE with both electrodes. Figure 5a shows the charge and discharge curves of the NCM811/Li cell for the first two cycles in the voltage range of 3.0–4.3V at a rate of 0.5 C at room temperature. The initial charge and discharge capacities are respectively 151 mAh/g and 130 mAh/g with Coulombic efficiency of 86.5%. Remarkably, NCM811/Li cell based on LLZO-IL electrolyte shows comparable voltage platform to that based on commercial liquid electrolyte, as shown in Figure S2. The similar behavior is shown in $LiFePO_4$/Li cell (Figure 5d). The low polarization voltage in solid state battery can be attributed to the high ionic conductivity of the electrolyte and small interfacial resistance between electrolyte and anode/cathode.[41] Figure S3a shows the CV curves of the initial three cycles of the $LiFePO_4$/LLZO-IL/Li cell at a scanning rate of 2 mV/s from 2 V to 5 V. A stable reversible curve is observed after the 2nd cycle. The resistance (Figure S3b) after the CV test only slightly increases. In addition, LLZO-IL HSE is stable with the oxide cathode at high voltage. Figure S4 displays time dependent impedance plot for the $LiFePO_4$/LLZO-IL/Li cell charged at a constant voltage of 4.2 V. The total resistance maintains a negligible increase when charging at 4.2 V. These results confirm that BMP-TFSI coating layer provides an excellent conducting medium for fast ion transport.

Figure 5b displays the cycling performance of the NCM811/Li cell at a rate of 0.5 C. The NCM811/LLZO-IL/Li cell demonstrates a high reversible capacity of 150

mAh/g at beginning and 102 mAh/g after 200 cycles. The cycling performance for solid state cell based on LLZO-IL HSE is comparable to those based on liquid electrolytes.[42] Regarding the $LiFePO_4$/LLZO-IL/Li cell (Figure 5e), a discharge specific capacity of 119 mAh/g without capacity loss after 60 cycles is achieved. Except the first few cycles, the Coulombic efficiency is close to 99%. The rate performance of the NCM811/LLZO-IL/Li cell is shown in Figure 5c. The cell provides a discharge capacity of 187 mAh/g at 0.1 C, 164 mAh/g at 0.2 C, 134 mAh/g at 0.5 C, 116mAh/g at 1 C, and below 100mAh/g at the current over 2 C, indicating an excellent rate capability in solid state batteries. The $LiFePO_4$/LLZO-IL/Li cell also demonstrates a good rate capability, as shown in Figure 5f.

Figure 6 compares the specific discharge capacity of the $LiFePO_4$/Li cells with various electrolytes. It can be clearly seen that the specific capacities of the cell based on LLZO-IL HSE at all C rates are higher than those of the cells based on 0.5M LiTFSI/BMP-TFSI and 0.5M $LiPF_6$/BMP-TFSI IL-based electrolytes.[11c] The difference is significantly enlarged at higher C rate. This mainly originates from the identical Li^+ transference number and faster Li ion transport in LLZO-IL HSE in contrast to the IL electrolytes. The superior electrochemical performance of HSE-based solid state batteries confirms that the interface between LLZO-IL HSE and metallic lithium is considerably stable; LLZO-IL HSE is compatible toward both oxide cathodes and metallic Li.

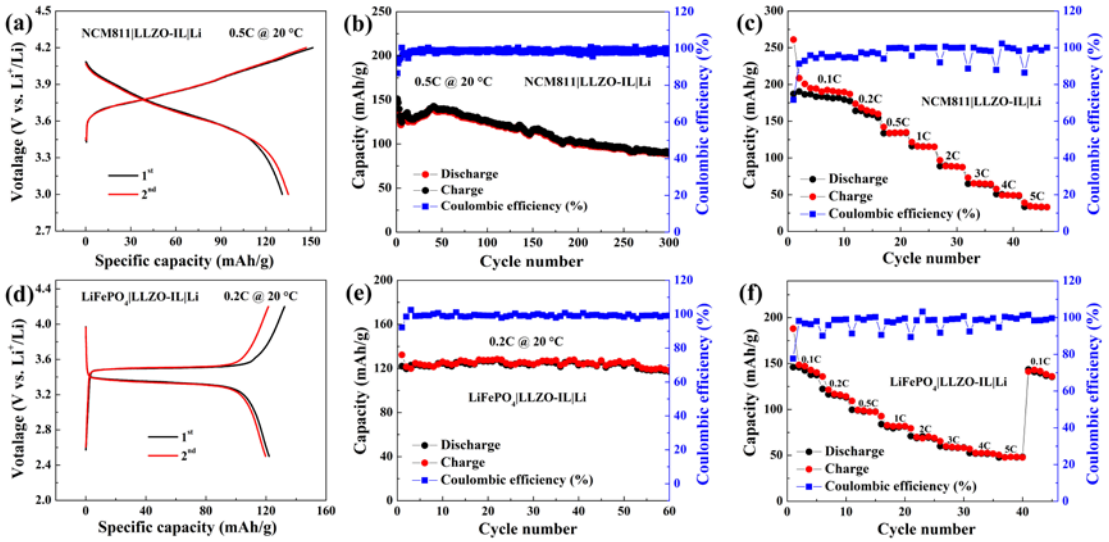

Figure 5. Charge-discharge curves (a) and cycling stability (b) of the NCM811/LLZO-IL/Li cell at a current density of 0.5 C at room temperature. (c) Rate performance of NCM811/LLZO-IL/Li cell at current densities of 0.1 C–5 C. Charge-discharge curves (d) and cycling stability (e) of the $LiFePO_4$/LLZO-IL/Li cell at a current density of 0.2 C at room temperature. (f) Rate performance of $LiFePO_4$/LLZO-IL/Li cell at current densities of 0.1 C–5 C.

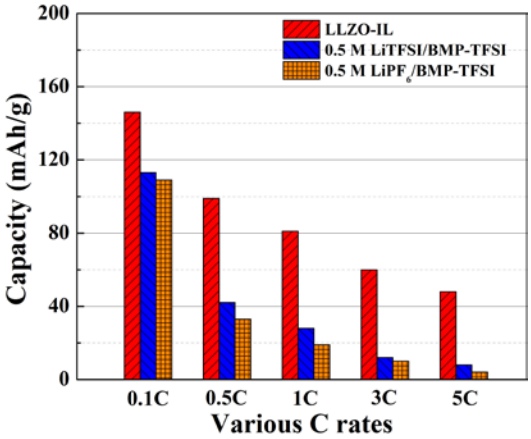

Figure 6. The histogram of discharge specific capacity at various C rates for the $LiFePO_4$/Li cell based on LLZO-IL HSE and compared with those based on IL electrolytes.[11c]

4. CONCLUSIONS

In summary, a facial method was designed to improve the interfacial performance of cubic LLZO sintered at 900 °C through incorporating BMP-TFSI IL with no added Li-salt. The XRD, Raman, and FTIR results reveal that LLZO is stable with BMP-TFSI IL. The "soft" consecutive BMP-TFSI coating layer not only compacts the microstructure and resists the volume strain, more important, forms a conducting network facilitating Li^+ transport, which changes the Li^+ conduction mode from point contacts to face contacts. In addition, no added Li-salt in BMP-TFSI ensures a high Li^+ transference numbers and maintains a low viscosity to facilitate Li^+ transport. As a result, even with slight IL incorporation, the ionic conductivity of LLZO is intensively enhanced by three orders of magnitude. Considering the ionic conductivity and the formability, the HSE with 14 wt% BMP-TFSI (LLZO-IL) is regarded as an optimized component. The improved ionic conductivity is attributed to the intensively reduced grain boundary resistance. More important, LLZO-IL exhibits good interfacial compatibility and interfacial wettability toward metallic Li, thus decreasing the interfacial resistance of electrolyte/Li. In parallel, the consecutive coating layer in LLZO-IL significantly suppresses the Li dendrite growth. Along with an broad electrochemical window over 5.5 V and a Li^+ transference number practically reaching unity, the NCM811/Li and $LiFePO_4$/Li solid batteries with LLZO-IL HSE demonstrate superior cycling stability and low polarization comparable to those with commercial liquid electrolytes, and excellent rate capability better than those with Li-salt-based ionic liquid electrolytes. Interfacial architecture engineering by IL-incorporation provides a new strategy for oxide-based solid electrolytes with good

overall performance avoiding high temperature sintering.

ASSOCIATED CONTENT

Supporting Information

The Supporting Information is available free of charge on the ACS Publications website at DOI: XXX.

Nyquist plots of the Li/LLZO-IL/Li symmetric cell, charge-discharge curves of the NCM811/Li cells with various electrolytes, CV curves and AC impedance spectra for the $LiFePO_4$/LLZO-IL/Li cell, stability of LLZO-IL against $LiFePO_4$ at a constant voltage of 4.2 V (PDF).

AUTHOR INFORMATION

Corresponding Author

*E-mail: lzhang@ysu.edu.cn. Phone: +86 335 8057047. Fax:+86 335 8074545.

ORCID

Long Zhang: 0000-0002-4861-1471

Notes

The authors declare no competing financial interest.

ACKNOWLEDGMENTS

This work was supported by the Science Foundation of Hebei Education Department (ZD2016033) and Natural Science Foundation of Hebei Province (E2018203301).

REFERENCES

[1] A. Manthiram, X. Yu, S. Wang, *Nat. Rev. Mater.* **2017,** *2*, 16103.

[2] a) L. Fan, S. Wei, S. Li, Q. Li, Y. Lu, *Adv. Energy Mater.* **2018,** *8*, 1702657; b) B. Zheng, H. Wang, J. Ma, Z. Gong, Y. Yang, *Sci. Sin.: Chim.* **2017,** *47*, 579-593; c) C. Yang, K. Fu, Y. Zhang, E. Hitz, L. Hu, *Adv. Mater.* **2017**, *29*, 1701169.

[3] a) J. Ma, B. Chen, L. Wang, G. Cui, *J. Power Sources* **2018,** *392*, 94-115; b) F. Zheng, M. Kotobuki, S. Song, M. O. Lai, L. Lu, *J. Power Sources* **2018,** *389*, 198-213; c) C. Sun, J. Liu, Y. Gong, D. P. Wilkinson, J. Zhang, *Nano Energy* **2017**, *33*, 363-386; d) B. Zhang, R. Tan, L. Yang, J. Zheng, K. Zhang, S. Mo, Z. Lin, F. Pan, *Energy Storage Mater.* **2018,** *10*, 139-159; e) Q. Liu, Z. Geng, C. Han, Y. Fu, S. Li, Y.-b. He, F. Kang, B. Li, *J. Power Sources* **2018,** *389*, 120-134.

[4] R. Murugan, V. Thangadurai, W. Weppner, *Angew. Chem.* **2007,** *46*, 7778-7781.

[5] a) S. Ramakumar, C. Deviannapoorani, L. Dhivya, L. S. Shankar, R. Murugan, *Prog. Mater. Sci.* **2017,** *88*, 325-411; b) V. Thangadurai, S. Narayanan, D. Pinzaru, *Chem. Soc. Rev.* **2014,** *43*, 4714-4727; c) Y. Ren, K. Chen, R. Chen, T. Liu, Y. Zhang, C.-W. Nan, B. Vyas, *J. Am. Ceram. Soc.* **2015,** *98*, 3603-3623; d) H. Duan, H. Zheng, Y. Zhou, B. Xu, H. Liu, *Solid State Ionics* **2018**, *318*, 45-53.

[6] a) X. B. Cheng, R. Zhang, C. Z. Zhao, Q. Zhang, *Chem.Rev.* **2017,** *117*, 10403-10473; b) Y. Liu, P. He, H. Zhou, *Adv. Energy Mater.* **2017,** *8*, 1701602.

[7] K. Kerman, A. Luntz, V. Viswanathan, Y.-M. Chiang, Z. Chen, *J. Electrochem. Soc.* **2017,** *164*, A1731-A1744.

[8] J. Awaka, N. Kijima, H. Hayakawa, J. Akimoto, *J. Solid State Chem.* **2009,** *182*, 2046-2052.

[9] J. Awaka, A. Takashima, H. Hayakawa, N. Kijima, Y. Idemoto, J. Akimoto, *Key Eng. Mater.* **2011,** *485*, 99-102.

[10] M. R. Busche, T. Drossel, T. Leichtweiss, D. A. Weber, M. Falk, M. Schneider, M. L. Reich, H. Sommer, P. Adelhelm, J. Janek, *Nat. Chem.* **2016,** *8*, 426-434.

[11] a) M. Galiński, A. Lewandowski, I. Stępniak, *Electrochim. Acta* **2006,** *51*, 5567-5580; b) M. Armand, F. Endres, D. R. Macfarlane, H. Ohno, B. Scrosati, *Nat. Mater.* **2009,** *8*, 621-9; c) N. Wongittharom, T.-C. Lee, C.-H. Hsu, G. Ting-Kuo Fey, K.-P. Huang, J.-K. Chang, *J. Power Sources* **2013**, *240*, 676-682.

[12] M. Egashira, H. Todo, N. Yoshimoto, M. Morita, J.-I. Yamaki, *J. Power Sources* **2007,** *174*, 560-564.

[13] T. Frömling, M. Kunze, M. Schönhoff, J. Sundermeyer, B. Roling, *J. Phys. Chem. B* **2008**, *112*, 12985-12990.

[14] M. J. Monteiro, F. F. Bazito, L. J. Siqueira, M. C. Ribeiro, R. M. Torresi, *J. Phys. Chem. B* **2008**, *112*, 2102-2109.

[15] a) C. J. Allen, J. Hwang, R. Kautz, S. Mukerjee, E. J. Plichta, M. A. Hendrickson, K. M. Abraham, *J. Phys. Chem. C* **2012,** *116*, 20755-20764; b) J. Zheng, M. Gu, H. Chen, P. Meduri, M. H. Engelhard, J.-G. Zhang, J. Liu, J. Xiao, *J. Mater. Chem. A* **2013,** *1*, 8464-8470.

[16] X. Pan, L. Fang, H. Guan, H. Yi, *Chemistry* **2014,** *77*, 752-759.

[17] G. B. Appetecchi, M. Montanino, D. Zane, M. Carewska, F. Alessandrini, S. Passerini, *Electrochim. Acta* **2009**, *54*, 1325-1332.

[18] Y. Li, Z. Wang, C. Li, Y. Cao, X. Guo, *J. Power Sources* **2014,** *248*, 642-646.

[19] a) Y. Li, B. Xu, H. Xu, H. Duan, X. Lu, S. Xin, W. Zhou, L. Xue, G. Fu, A. Manthiram, J. B. Goodenough, *Angew. Chem.* **2017,** *56*, 753-756; b) L. Dhivya, R. Murugan, *ACS Appl. Mater. Interfaces* **2014,** *6*, 17606-17615.

[20] Y. Seino, T. Ota, K. Takada, A. Hayashi, M. Tatsumisago, *Energy Environ. Sci.* **2014**, *7*, 627-631.

[21] B. Xu, H. Duan, H. Liu, C. A. Wang, S. Zhong, *ACS appl. mater. interfaces* **2017,** *9*,

21077-21082.

[22] F. Tietz, T. Wegener, M. T. Gerhards, M. Giarola, G. Mariotto, *Solid State Ionics* **2013**, *230*, 77-82.

[23] Y. Umebayashi, T. Mitsugi, S. Fukuda, T. Fujimori, K. Fujii, R. Kanzaki, M. Takeuchi, S. Ishiguro, *J. Phys. Chem. B* **2007,** *111*, 13028-13032.

[24] W. Na, A. S. Lee, J. H. Lee, S. S. Hwang, S. M. Hong, E. Kim, C. M. Koo, *Electrochim. Acta* **2016,** *188*, 582-588.

[25] M. R. Busche, T. Drossel, T. Leichtweiss, D. A. Weber, M. Falk, M. Schneider, M.-L. Reich, H. Sommer, P. Adelhelm, J. Janek, *Nat. chem.* **2016,** *8*, 426–434.

[26] a) A. Sharafi, S. Yu, M. Naguib, M. Lee, C. Ma, H. M. Meyer, J. Nanda, M. Chi, D. J. Siegel, J. Sakamoto, *J. Mater. Chem. A* **2017**, *5*, 13475-13487; b) Y. Li, X. Chen, A. Dolocan, Z. Cui, S. Xin, L. Xue, H. Xu, K. Park, J. B. Goodenough, *J. Am. Chem. Soc.* **2018**, *140*, 6448-6455; c) L. Cheng, E. J. Crumlin, W. Chen, R. Qiao, H. Hou, S. Franz Lux, V. Zorba, R. Russo, R. Kostecki, Z. Liu, K. Persson, W. Yang, J. Cabana, T. Richardson, G. Chen, M. Doeff, *Phys. Chem. Chem. Phys.* **2014**, *16*, 18294-18300.

[27] a) M. Laporta, M. Pegoraro, L. Zanderighi, *Phys. Chem. Chem. Phys.* **1999,** *1*, 4619-4628; b) W. Xia, B. Xu, H. Duan, X. Tang, Y. Guo, H. Kang, H. Li, H. Liu, *J. Am. Ceram. Soc.* **2017,** *100*, 2832-2839.

[28] C. Liu, K. Rui, C. Shen, M. E. Badding, G. Zhang, Z. Wen, *J. Power Sources* **2015,** *282*, 286-293.

[29] E. Markevich, R. Sharabi, V. Borgel, H. Gottlieb, G. Salitra, D. Aurbach, G. Semrau, M. A. Schmidt, *Electrochim. Acta* **2010,** *55*, 2687-2696.

[30] S. M. Mohd Razalli, S. I. Y. Sheikh Mohd Saaid, A. M. Marwan Ali, O. H. Hassan, M. Z. A. Yahya, *Funct. Mater. Lett.* **2015,** *08*, 1540017.

[31] a) M. H. Hebb, *J. Chem. Phys.* **1952,** *20*, 185-190; b) C. Wagner, *J. Chem. Phys.* **1953,** *21*, 1819-1827.

[32] a) L. Zhang, D. Zhang, K. Yang, X. Yan, L. Wang, J. Mi, B. Xu, Y. Li, *Adv. Sci.* **2016,** *3*, 1600089; b) L. Zhang, K. Yang, J. Mi, L. Lu, L. Zhao, L. Wang, Y. Li, H. Zeng, *Adv. Energy Mater.* **2015,** *5*, 1501294.

[33] R. Garcia-Mendez, F. Mizuno, R. Zhang, T. S. Arthur, J. Sakamoto, *Electrochim. Acta* **2017,** *237*, 144-151.

[34] M. Kotobuki, H. Munakata, K. Kanamura, Y. Sato, T. Yoshida, *J. Electrochem. Soc.* **2010,** *157*, A1076- A1079.

[35] a) F. Yonemoto, A. Nishimura, M. Motoyama, N. Tsuchimine, S. Kobayashi, Y. Iriyama, *J. Power Sources* **2017,** *343*, 207-215; b) K. Fu, Y. Gong, B. Liu, Y. Zhu, S. Xu, Y. Yao, W. Luo, C. Wang, S. D. Lacey, J. Dai, Y. Chen, Y. Mo, E. Wachsman, L. Hu, *Sci. Adv.* **2017,** *3*, e1601659; c) C. L. Tsai, V. Roddatis, C. V. Chandran, Q. Ma, S. Uhlenbruck, M. Bram, P. Heitjans, O. Guillon, *ACS appl. mater. interfaces* **2016,** *8*, 10617-10626; d) W. Luo, Y. Gong, Y. Zhu, Y. Li, Y. Yao, Y. Zhang, K. Fu, G. Pastel, C.-F. Lin, Y. Mo, E. D. Wachsman, L. Hu, *Adv. Mater.* **2017**, *29*, 1606042.

[36] a) L. Cheng, W. Chen, M. Kunz, K. Persson, N. Tamura, G. Chen, M. Doeff, *ACS Appl. Mater. Interfaces* **2015,** *7*, 2073-2081; b) R. Hongahally Basappa, T. Ito, T. Morimura, R. Bekarevich, K. Mitsuishi, H. Yamada, *J. Power Sources* **2017,** *363*, 145-152.

[37] Z. Deng, Z. Wang, I.-H. Chu, J. Luo, S. P. Ong, *J. Electrochem. Soc.* **2015,** *163*, A67-A74.

[38] M. He, Z. Cui, C. Chen, Y. Li, X. Guo, *J. Mater. Chem. A* **2018**, *6*, 11463-11470.

[39] a) K. Park, B.-C. Yu, J.-W. Jung, Y. Li, W. Zhou, H. Gao, S. Son, J. B. Goodenough, *Chem. Mater.* **2016,** *28*, 8051-8059; b) Y. Ren, Y. Shen, Y. Lin, C.-W. Nan, *Electrochem. Commun.* **2015,** *57*, 27-30.

[40] W. Zhou, S. Wang, Y. Li, S. Xin, A. Manthiram, J. B. Goodenough, *J. Am. Chem. Soc.* **2016,** *138*, 9385-9388.

[41] a) Q. Lu, J. Fang, J. Yang, G. Yan, S. Liu, J. Wang, *J. Memb. Sci.* **2013,** *425-426*, 105-112; b) Y. Li, H. Xu, P. H. Chien, N. Wu, S. Xin, L. Xue, K. Park, Y. Y. Hu, J. B. Goodenough, *Angew. Chem.* **2018**, *57*, 8587-8591.

[42] F. Schipper, H. Bouzaglo, M. Dixit, E. M. Erickson, T. Weigel, M. Talianker, J. Grinblat, L. Burstein, M. Schmidt, J. Lampert, C. Erk, B. Markovsky, D. T. Major, D. Aurbach, *Adv. Energy Mater.* **2018,** *8*, 1701682.

10.1002/cssc.201801756

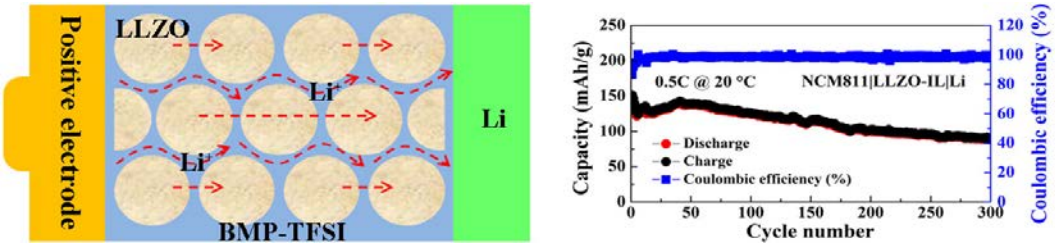

Table of Contents/Abstract Graphic